Immune responses in pancreatic cancer may be restricted by prevalence of activated regulatory T-cells, dysfunctional CD8+ T-cells, and senescent T-cells

Shivan Sivakumar[1,2,3]*, Enas Abu-Shah[2,4]*§, David J Ahern[2], Edward H Arbe-Barnes[5], Nagina Mangal[6], Srikanth Reddy[3], Aniko Rendek[3], Alistair Easton[1], Elke Kurz[2], Michael Silva[3], Lara R Heij[7,8], Zahir Soonawalla[3], Rachael Bashford- Rogers[9], Mark R Middleton[1,3+], Michael L Dustin[2+§]

[1] Department of Oncology, University of Oxford, Oxford OX3 7DQ, UK. [2] Kennedy Institute of Rheumatology, University of Oxford, Oxford OX3 7FY, UK. [3] University Hospitals NHS foundations Trust, Oxford, UK. [4] Sir William Dunn School of Pathology, University of Oxford, Oxford OX1 3RE, UK. [5] University of Oxford Medical School. [6] Nuffield Department of Surgical Sciences, University of Oxford, Oxford OX3 9DU, UK. [7] Department of General, Gastrointestinal, Hepatobiliary and Transplant Surgery, RWTH Aachen University Hospital, Aachen Germany. [8] Institute of Pathology, University Hospital RWTH Aachen, Aachen, Germany. [9] Wellcome Trust Centre for Human Genomics, University of Oxford, Oxford OX3 7BN, UK.

* Those authors contributed equally to the work. + These authors jointly directed the work. § correspondence should be addressed to: enas.abushah@path.ox.ac.uk, or michael.dustin@kennedy.ox.ac.uk

Abstract

Pancreatic cancer has the worst prognosis of any human malignancy and lymphocytes appear to be a major prognostic marker of the disease. There is a need to better characterise T-cells of pancreatic cancer in order to identify novel therapeutic strategies. In this study, a multi-parameter analysis of human pancreatic cancer cases revealed three novel characteristics of T-cells. Using a T-cell focused CyTOF panel, we analysed approximately 32,000 T-cells in eight patients. Our observations show a regulatory T-cell population was characterized by a highly immunosuppressive state with high TIGIT and ICOS expression, and the CD8 T-cells were either senescent or exhausted but with lower PD1 levels. These data suggest that the microenvironment of pancreatic cancer is extremely suppressive and could be a major driver of poor prognosis. These findings have been subsequently validated in a large pancreatic cancer single-cell RNA sequencing dataset using 13,000 T cells. This work identifies potential therapeutic targets and avenues that should be further investigated through rational design of clinical trials.

Introduction

Pancreatic ductal adenocarcinoma (PDAC) has the worst survival of any human cancer with the survival being approximately 7% (1). Early diagnosis with surgical resection and adjuvant folfirinox offers the best chance of cure for these patients (2). We and others have recently shown that the immune infiltrate in the primary pancreatic tumour can predict prognosis after a surgical resection (3,4). There is now demonstrable evidence that pancreatic cancer has a complex immune microenvironment with T-cells, macrophages, neutrophils, NK cells, B-cells and dendritic cells involved (3,5-7). Checkpoint immunotherapy (especially PD-1) has demonstrably improved the prognosis of melanoma and lung cancer (8,9), in which it takes the 'brakes' off T-cells. However, checkpoint blockade trials have had minimal effects on prognosis in pancreatic cancer, with no durable response, and only a sub-group of patients respond(10-12). It is now well-established that PDAC is infiltrated by $CD4^+$, $CD8^+$ and Regulatory T-cells (Tregs)(13,14).

Due to the poor response of checkpoint blockade agents in PDAC, it would be appropriate to take a step back and characterise the states and specific populations of T-cells in this disease, which is the broad scope of this paper. Even though we know T-cells exist in the microenvironment of pancreatic cancer, not much is known about their differentiation or activation status. Furthermore, cancer therapeutics has been dominated by PD-1 and CTLA blocking antibodies but other checkpoints, such as TIGIT, Tim3, Lag3 and CD39, have been identified in recent years, calling for revisiting their roles in PDAC. There are also checkpoint co-stimulatory molecules such as ICOS, OX40, CD40L, GITR and 4-1BB.

In this study we have aimed to characterise the immune landscape and specifically T-cells, and their checkpoint expression patterns in pancreatic cancer patients in the hope of understanding the features to aid rational drug development and novel therapeutics for this disease.

Results

Rich, but tumour supportive, innate immune composition within pancreatic cancer

We have designed our study to interrogate the immune landscape within primary pancreatic tumours with an in-depth characterisation of its T-cells' functional states. To that end, we have used fresh samples from resectable tumours (Table 1) and matched blood samples. Tissues were processed within 2 hours of the operation and made into single cell suspensions stained with a cocktail of mass-cytometry (CyTOF) antibodies for the main immune lineage markers, and cellular states (Fig. 1a, Table 2). Unsurprisingly, we observed a certain degree of heterogeneity in the cellular composition of the tumours with the major component being the stroma (Fig.1b). This is in concordance with the fibrotic nature of PDAC (15). It is, however, evident that all 8 patients analysed, exhibited a substantial level of immune cell involvement, observed from the $CD45_{+}$ signature, which varied between 5-45% of all live cells.

Our panel allowed us to identify the main immune cell lineages, and this is illustrated in the viSNE plot and marker expression maps (Fig. 1c). Using unsupervised hierarchical clustering (FLOWSOM), we identified the different clusters of cells corresponding to the different lineages (Fig. 1d; viSNE and heatmap). There were multiple shared features across all patients including the presence of $CD4_{+}$ T-cells (cluster 11), $CD8_{+}$ T-cells (cluster 7), granulocytes (clusters 8,10,12) and mononuclear phagocytes (clusters 1,2,4,5). It is interesting to note however that both B-cells (cluster 3) and NK cells (cluster 9) can be completely absent in some patients. It is possible to appreciate the degree of patient variability by inspecting the individual clustering trees for each patient (Fig. S1), where it is evident that patient 3 lacks any B-cells and patient 9 lacks NK cells (Fig. S2b).

We have then identified several subsets of NK cells (Fig. 1e, Fig. S2), granulocytes (Fig. 1f, Fig. S3) and mononuclear phagocytes (Fig. 1g, Fig. S4). It is particularly striking to see that most NK clusters express the inhibitory molecule TIGIT at varying levels, with those having the highest expression being granzyme B negative, indicating a defective killing capacity (clusters 1,3,4,6,10). These cells are also tissue resident, as identified by the expression of the adhesion molecule CD103. On the other hand, the infiltrating NK populations have higher cytotoxic state with CD16, CD57 and granzyme B expression (clusters 5,7,8,9).

The majority of the granulocyte cluster are $CD15_{+}CD16_{+}CD14_{\pm}$, corresponding to granulocyte myeloid-derived suppressor cells (G-MDSC) (16,17) or antigen-presenting tumour associated neutrophils (18) marked by their HLA-DR and PD-L1 expression (cluster 1).

In the myeloid compartment we could identify some MDSCs expressing low levels of HLA-DR and high PD-L1 (cluster 6,9), while the major population appears to be with intact antigen presentation capabilities ($HLAD\text{-}DR_{++}$, cluster 2). This is in contrast to previous reports that suggested the majority of infiltrating myeloid cells in PDAC to be MDSC (16,19).

Peripheral blood from the same patients presented different population compositions (Fig. S5). Specifically, we only observed a small percentage (<2%) of low-density neutrophils in the PBMC samples (Fig. S5a, cluster 11,14) which have been described in other tumours (20). Circulating NK cells, unlike the tumour-associated ones, appear to retain their cytolytic activity with most sub-populations being $CD56_{dim}$, $CD57_{+}$, granzyme B_{+} and $CD16_{+}$ (Fig. S5b). We also observed a

significant population of circulating MDSCs (Fig. S5a, cluster 3) and the presence of T-cell/monocyte complexes indicating an immune perturbation (21) (Fig. S5a, cluster 2,13), those specifically express PD-L1 (Fig. S5c, cluster 1).

T-cells are either suppressive or non-responsive in PDAC tumours

As many immunotherapies are targeted against T-cells, but yet have failed to show significant clinical benefit in PDAC, we hypothesised that the pathways that have been targeted thus far may not be dominant in PDAC which warrants a revised mapping of the T-cell's state in the tumour microenvironment. To that end, we have analysed the functional states of CD3+ T-cells from the tumours using a set of differentiation and activation markers in combination with checkpoint antibodies, to characterise the CD8+ (Fig. 2a), CD4+ (Fig. 2b) and Treg (Fig. 2c) compartments.

We have identified 30 distinct clusters of CD8+ T-cells, among which was a prominent senescent cluster characterised as CD57+CD27-CD28- which have been extensively discussed in the context of aging and viral infections as a subset of T-cells suffering from proliferation senescence and reduced T-cell signalling while maintaining their cytolytic capabilities (22,23). They are only recently gaining attention in the context of cancer (24,25), and this is the first report to describe them in pancreatic cancer. Despite the presence of this population we have also identified a handful of clusters with activated status (cluster 2,27), proliferating (cluster 28,29), and cytotoxic (cluster 6,7,10,15). Two additional negative regulators were a cluster of FoxP3+ CD8+ "regulatory" T-cells (cluster 30), which is only present in 2 out of the 8 patients (Fig. S6), and an exhausted population expressing high levels of multiple inhibitory receptors (cluster 4,5,9). Interestingly, PD1 expression on the exhausted cluster was low which could explain the limited clinical success targeting this axis. Overall, we can identify that ~ 17.75±2.72% (mean ±s.d) of the CD8+ T-cells are potentiating anti-tumour responses while ~ 37.34±4.05% are either unresponsive (naïve, senescent or exhausted) or even inhibitory. This suggests a certain degree of anti-tumour potential of the CD8+ compartment that seems to be inhibited by other factors preventing the control of the disease.

We have therefore assessed the contribution from CD4+ T-cells to support CD8+ T-cells (Fig. 2b). It was evident from this analysis that the 17 identified clusters can be divided into two groups: (1) senescent or non-tumour responsive (~78.8±5.96%) and (2) regulatory (~18.52±2.69%), spanning up to 45% of the CD4+ population in certain patients (Fig. S7).

We finally sought to characterise the Treg subsets within the tumours (Fig. 2c, Fig. S8), which further supported our hypothesis that an inhibitory microenvironment could be stopping any productive CD8+-mediated anti-tumour responses. We discovered that the majority of the Tregs (~54.45±4.79%) showed signs of functional activation and high suppression capacity. They expressed the TNF family receptor 41BB and the inhibitory receptors PD-1, PD-L1 and HLA-DR. Some have acquired cytotoxic activity (CD57+, cluster 12) while the most prominent ones have high expression of TIGIT and ICOS, indicative of superior inhibitory activity (26-28).

In the periphery, the CD8+ T-cells also exhibited a significant senescent population (Fig. S9, cluster 4) although we could identify a small population of activated and proliferating cells (Ki67+41BB+HLADR+, cluster 7,8). The CD4+ T-cells showed immune complexes with monocytes (CD3+CD4+CD14+, Fig. S9b, cluster 11) but many of the cells are naive or non-activated. However, there is a small fraction of

cytotoxic cells (Granzyme B+, cluster 2,7). The Tregs in the circulation are also characterised by the high levels of TIGIT expression albeit at lower levels compared to the tumour-associated populations (~30% higher median expression). There is a larger naive population (CCR7+CD45RA+) compared to the tumour [13.2±5.466% vs 6.56±3.75%].

Single-cell RNA sequencing identifies senescence and regulatory signatures in tumour infiltrating T-cells

Senescent T-cells and TIGIT+ICOS+ Tregs are two novel findings in pancreatic cancer. We have therefore independently validated these results by re-analysing a publicly available single-cell RNA sequencing resource from 24 PDAC patients (29) (Fig. 3). By focusing only on the T-cell compartment in that data set we identified 200 unique clusters as shown in the UMAP (Fig. 3a) corresponding to CD8+ and CD4+ T-cells as well as some non-conventional T-cells. We were able to identify 13 Treg clusters based on Foxp3+ expression, all of which exhibit high expression levels of *TIGIT* and co-expressing *ICOS* and CD39 (*ENTPD1*) (Fig. 3b, violin plots, supplemental data 1). We also identified 6 clusters of senescent T-cells (Fig. 3c) characterised by increased NK marker expression (*KLRG1, KLRB1*) and senescent markers (*HCST*, *HMGB1*) (23). Complete differential expression analysis of those populations relative to other CD4+ and CD8+ T-cells can be found in supplemental data 2.

Finally, we also identified the exhausted cells cluster which was captured by requiring the co-expression of at least 3 of the known exhaustion signature genes *PDCD1, TIM3, LAG3, TIGIT, CTLA4 and ENTPD1*, (Fig. 3d). This allowed us to capture the exhausted clusters with low *PDCD1* expression (Fig. 3d violin plot cluster 35, 85, 96, 161). Interestingly, previously reported exhaustion genes such as *TOX* (30), *LAYN* and *MIR155HC* (31), were only upregulated in some of the exhausted clusters suggesting a unique exhaustion signature in PDAC.

Effector T-cells are uniformly distributed within pancreatic tumour, but Tregs are restricted to the stroma

In order to shed light into potential cellular communications between different T-cell subsets and the surrounding malignant epithelium of the tumour we have analysed their spatial distribution using multiplex immunofluorescence (IF) on formalin-fixed paraffin embedded (FFPE) sections from the same patients (Fig. 4). For each case we identified the cancer, pancreatitis and normal pancreas where available (Fig. 4a-c respectively) and annotated the regions into epithelium (based on pan Cytokeratin staining) and Stroma (based on αSMA staining). Using the expression of the canonical T-cell markers (CD3+, CD4+, CD8+ and Foxp3+), we identified their respective cellular subsets (Fig. S10). When analysing CD4+ and CD8+ distribution within the different regions of the tissue (Fig. 4d) we noticed they were homogeneously distributed with no signs of being excluded from the tumour core. On the other hand, Tregs were exclusively restricted to the stroma and almost absent from the cancer regions. This supports recent reports suggesting an interplay between Tregs and fibroblasts in PDAC (32). A finer analysis of their distribution within stroma of different densities defined by αSMA signal did not reveal any preferential localisation

(Fig. S10b). To further elucidate the relationships between the cells we performed proximity analysis that revealed the majority of CD8+ T-cells were localised within 50 μm of the epithelium, and there is some indication of lower numbers within the cancer region albeit not statistically significant (Fig. 4e). 90% of Tregs were in close proximity of a CD8+ T-cell, potentially facilitating their suppressive activity (Fig. 4f).

Discussion

Here we report for the first time an in-depth immune landscape characterisation of primary human pancreatic ductal adenocarcinoma, that has revealed multiple distinct signatures of this tumour with potential for revolutionising the therapeutic approach. It is clear that the tumour microenvironment is immuno-suppressive and we have provided further evidence supporting this by identifying the presence of dysfunctional NK cells, granulocyte and myeloid MDSCs present (Figure 1). However, our study focused predominantly on T-cells as they are the targets of current checkpoint therapeutics. Despite the lack of survival benefit from checkpoint blockades in pancreatic cancer, we see a response rate of 5-10% in trials.

There are clear signatures of dysfunctional effector T-cell populations which are present in both the CD8+ and CD4+ compartments. The first is an exhausted signature which, surprisingly, is not characterised by high PD1 expression but by a different set of inhibitory molecules including TIGIT, CD39 and Tim3 (Figure 2a, Figure 3c). This finding again offers alternative therapeutic avenues to the previously unsuccessful approaches targeting the PD1/PDL1 axis.

It is well-established that Tregs are present in the PDAC microenvironment, but their functional characteristics are poorly understood. We identified a highly suppressive Treg population expressing the inhibitory molecule TIGIT and co-stimulatory molecule ICOS (Figure 2c, Figure 3b). Interestingly, these molecules were co-expressed in a large proportion of the Tregs. There are currently multiple blocking antibodies in development against these checkpoint molecules, and our data calls for trialling them in PDAC. This regulatory population is restricted to the stroma (Figure 4d), opening many questions regarding their interactions with fibroblasts and their potential implication in disease progression.

Finally, we identified a novel senescence signature which unlike the exhausted phenotype cannot benefit from checkpoint blockade approaches. T-cell senescence has been discussed in the context of viral infections, aging and CAR T-cell therapies and different avenues to replace or rejuvenate those cells through cell therapy and engineering are being investigated (33). It would be interesting to understand the cause of the observed senescence and whether it is directly linked to the immune-suppressive activity of Tregs in the tumour microenvironment (34,35).

In summary, our data maps the T cell landscape of pancreatic cancer and we propose three novel therapeutic approaches to employ immunotherapies in this recalcitrant disease as well as further scientific investigation.

Methods

Patient recruitment

Samples were collected from 8 patients diagnosed with pancreatic adenocarcinoma (Table 1) that were fit for palliative operation. The 8 patients consisted of 5 males and

3 females and ranged from ages of 51 to 80. 7 out of 8 patients has adjuvant chemotherapy following the operation, patient 2 and 3 have died within 9 months of the operation while patients 4, 6 and 7 have recurred since. All patients were consented for this study via the Oxford Radcliffe biobank (09/H0606/5+5, project: 18/A031).

Sample Collection

From the patients described above, 20 ml blood was collected immediately before surgery into sodium heparin tubes (BD). Tissue samples were placed in RPMI media (Corning) on ice and were reviewed by a designated histopathologist who provided a 10mm by 10mm by 3mm piece for this study.

PBMC Isolation

Blood samples were processed within 4 h of collection. 20 ml of 2% FBS/PBS was added to 20 ml of whole blood. This was layered onto Ficoll-Plaque. Sample was centrifuged at 1300 x *g* for 20 min at the slowest acceleration and with break off. After centrifugation, the PBMC ring was removed using a pipette. The ring was topped up with 2% FBS/PBS and centrifuged again at 300 x *g*. Any excess red blood cells were lysed with ACK solution (Life Technologies, A1049201) and cells were washed again.

Tissue Digestion

Sample is initially mechanically digested using a scalpel into small pieces. The pieces are put into a 15 ml conical tube, with 9 ml of complete RMPI (10% FBS, 1% Pen/Strep and 1 mM Glutamine) and 1 ml of 10X hyaluronidase/collagenase solution (StemCell, 07912). A first round of digestion is done at 37 $_{o}$C for 30 min in a pre-warmed shaker. The supernatant is collected without disrupting the tissue and a fresh digestion media is added (10ml complete RPMI containing 200 U of collagenase IV (Lorne Lanoratories, LS004194), 100 μl/ml of DNAaseI (Sigma, DN25) and 0.5 U of universal nuclease (Pierce, 88702) for an additional 30 min of digestion as before. The supernatant is combined with the one from the first digestion step and the remaining tumour pieces are squeezed through a 100um tissue strainer with a further 10 ml of complete RPMI. The supernatants from all digestion steps are combined and centrifuged for 10 min at 300 x *g*. Any residual red blood cells are removed with ACK solution.

CyTOF sample preparation

Samples were directly taken following isolation for CyTOF staining. Lanthanide metal-labelled antibodies were obtained from Fluidigm or by conjugation of metal isotopes to purified antibodies using Maxpar Conjugation kits (Fluidigm)- See table 2 for detailed list of antibodies and clones. Cells were stained for surface markers for 20 min at room temperature followed by Intercalator-$_{103}$Rh (Fluidigm, 201103A) staining for dead cell exclusion, then cell fixation and permeabilization was performed using the Maxpar Nuclear Antigen Staining Buffer Set (Fluidigm, 201067). The Maxpar nuclear staining protocol was used for the simultaneous detection of cytoplasmic and nuclear targets (Ki67, CTLA4 and Foxp3), staining was done for 20 min at room temperature. The cells were washed and incubated with 0.125nM Intercalator-191Ir (Fluidigm, 201192A) diluted in PBS containing 2% formaldehyde, and stored at 4 $_{o}$C until acquisition.

CyTOF Data Acquisition
Immediately prior to acquisition, samples were washed once with PBS, once with de-ionized water and then resuspended at a concentration of 1 million cells/ml in deionized water containing a 1/20 dilution of EQ 4 Element Beads (Fluidigm, 201078). The samples were acquired on a CyTOF Helios mass cytometer at an event rate of <500 events/second. After acquisition, the data were normalized using bead-based normalization in the CyTOF software. Data were exported as FCS files for downstream. The data were gated to exclude residual normalization beads, debris, dead cells and doublets, leaving DNA^{+} Rh^{low} events for subsequent clustering and high dimensional analyses.

CyTOF Data Analysis:
Dimensionality reduction visualisation with viSNE and clustering with FLOWSOM were done using built in functions in cytobank. The number of clusters and metaclusters for the flowsom algorithm were reviewed by the researchers. Heatmaps of normalized marker expression, relative marker expression, and relative difference of population frequency were generated by cytobank and plotted using Prism (GraphPad) and heirarchial clustering of the heatmaps was performed using Morpheus from the Broad Institute (https://www.broadinstitute.org/cancer/software/morpheus/), as an average with 1- Pearson correlation as a parameter.

Collection of Histological Sections
Sections were cut on a Leica RM2235 at around 5 microns thickness, floated on a warm water bath, dissected using forceps to isolate the region of interest and lifted centrally onto TOMO slides (VWR, TOMO® 631-1128). Sections were air-dried.

Multiplex immunohistochemistry
Multiplex (MP) immunofluorescence (IF) staining was carried out on 4um thick formalin fixed paraffin embedded (FFPE) sections using the OPAL™ protocol (AKOYA Biosciences) on the Leica BOND RXm autostainer (Leica, Microsystems).
Six consecutive staining cycles were performed using the following 1ry Antibody-Opal fluorophore pairings: CD4 (clone 4B12, NCL-L-CD4-368 (Leica Novocastra) – Opal 520); CD8 (clone C8/144B, M7103 (DAKO Agilent) -Opal 570); CD3 (clone LN10, NCL-L-CD3-565 (Leica Novocastra) – Opal 540); FOXP3 (clone 236A/E7, ab20034 (Abcam) – Opal 620); Pan Cytokeratin (clone AE1/AE3, M3515 (DAKO Agilent) – Opal 650) and αSMA (rabbit polyclonal, ab5694 (Abcam) -Opal 690).
Primary (1ry) Antibodies were incubated for one hour and detected using the BOND™ Polymer Refine Detection System (DS9800, Leica Biosystems) as per manufacturer's instructions, substituting the DAB for the Opal fluorophores, with a 10 min incubation time and without the Haematoxylin step. Antigen retrieval at 100 ºC for 20 min, as per standard Leica protocol, with Epitope Retrieval (ER) Solution 2 (AR9640, Leica Biosystems) was performed before each 1ry antibody was applied. Slides were then mounted with VECTASHIELD® Vibrance™ Antifade Mounting Medium with DAPI (H-1800-10, Vector Laboratories. Whole slide scans and multispectral images (MSI) were obtained on the AKOYA Biosciences Vectra® Polaris™. Batch analysis of the MSIs from each case was performed with the inForm 2.4.8 software provided. Finally,

batched analysed MSIs were fused in HALO (Indica Labs), to produce a spectrally unmixed reconstructed whole tissue image, ready for analysis.
Cover slips were lifted post multiplex staining and CD68 (Clone PG-M1, Dako M0876) antibody was stained for chromogenically on the Leica BOND autostainer. Antigen retrieval at 100 ºC for 20 min with Epitope Retrieval Solution 2 (AR9640, Leica Biosystems); primary antibody incubation at 1/400 dilution for 30 min then detection using the BOND™ Polymer Refine Detection System (DS9800, Leica Biosystems) as per manufacturer's instructions.

Multiplex immunohistochemistry- Image Analysis
Scanned slides were analysed using Indica Labs HALO® (version 3.0.311.407) image analysis software. Multiplex and brightfield images were manually annotated by a pathologist, defining areas of pancreas, pancreatitis, pancreatic adenocarcinoma and lymph node. The pathologist taught an integrated Random Forrest Classifier module to segment the multiplex images into stroma and epithelium, with obvious areas artefactual staining manually excluded. A separate Random Forest Classifier algorithm was taught to segment tissue into areas of high, medium and low smooth muscle actin (αSMA) expression. Analysis and cell detection/phenotyping was done using Indica Labs - HighPlex FL v3.1.0 (fluorescent images) and Indica Labs – Multiplex IHC v2.1.1 (brightfield images). Cells were annotated based on their marker expression as follows: Epithelium (DAPI+ Cytokeratin+), CD4 helper (DAPI+CD4+), CD8 cytotoxic (DAPI+CD8+) and regulatory T-cell (DAPI+CD4+Foxp3+). Multiplex and brightfield images were registered and topological analysis was carried out using integrated proximity analysis modules. Statistical analysis was done using 2-way ANOVA in Prism (GraphPad).

Single-cell RNA sequencing analysis: Pre-processing, integration and batch correction
FastQ files for 24 PDAC and 11 normal samples were downloaded from the Genome Sequence Archive (https://bigd.big.ac.cn/search?dbId=gsa&q=CRA001160), count matrices were generated in Cell Ranger 3.1.0 as per the original paper (29). Raw count matrices were imported into the Seurat R package and merged (36). Cells with <200 and >2.5x1010 genes, <400 and > 1x1016 molecules, and >25% mitochondrial genes were excluded. Batch correction was performed in Harmony (37).

Single-cell RNA sequencing analysis: *Single cell clustering and annotation*
Uniform manifold approximation and projection (UMAP) was performed on the scRNAseq harmonised cell embeddings, upon which clustering was performed. 12 broad cell clusters were identified using reference pancreas and immune gene lists (supplemental data 3). The T-cell cluster was subsetted into a new Seurat object, and UMAP was re-performed using genes relevant to T cells to generate 250 clusters (supplemental table 4).
Mean and 75th percentile normalised count matrices were generated for these clusters. 75th percentile normalised counts were used for cluster identification for all genes except for *CD4* and *B3GAT1* (where, due to low gene capture (38) in all clusters, means were used). Cells with negative expression of any of *CD3D*, *CD3E*, *CD3G* were excluded to ensure only T-cells were analysed. Double negative cells were defined by negative 75th percentile expression of *CD8A* and *CD8B*, and negative mean expression of *CD4*. Double positive cells were defined by positive expression of these genes. The CD4+ T-cells were defined as the remaining clusters with positive mean expression of

CD4. The CD8+ T-cells were defined as the remaining clusters which co-express *CD8A* and *CD8B*. The following filters were used for cluster definitions of validated cell populations: Tregs (positive expression of *FOXP3*); Senescent (negative expression of *CD27* and *CD28*, positive 75th percentile expression of *KLRG1* and positive mean expression of *B3GAT1*); Exhausted (positive 75th quantile expression of ≥ 4 of *HAVCR2*, *PDCD1*, *TOX*, *LAG3*, *CTLA4*, *TIGIT*, *CD38*, *ENTPD1* and positive expression of TRDC was filtered out to exclude gamma-delta T-cells).

Single-cell RNA sequencing analysis: *Data analysis and figures*
Differential expression analysis was performed with the FindMarkers function in Seurat. Data for violin plots were extracted using for tumour samples only. Heatmaps and violin plots were generated in Prism (GraphPad) using matrices of 75th quantile and mean expression.

Disclosure of potential conflicts of interest

SS has salary and research expenses from BMS. EAS has salary from UCB. RJMB-R is a co-founder and consultant for Alchemab Therapeutics Ltd and a consultant for Imperial College London and VHSquared. MM reports personal fees from Amgen, grants and personal fees from Roche, grants from Astrazeneca, grants and personal fees from GSK, personal fees and other from Novartis, other from Millenium, personal fees, non-financial support and other from Immunocore, personal fees and other from BMS, personal fees and other from Eisai, other from Pfizer, personal fees, non-financial support and other from Merck/MSD, personal fees and other from Rigontec (acquired by MSD), other from Regeneron, personal fees from BiolineRx, personal fees and other from Array Biopharma (now Pfizer), non-financial support and other from Replimune, personal fees from Kineta, personal fees from Silicon Therapeutics, outside the submitted work.

Acknowledgements

We thank all members of the Dustin lab for fruitful discussions. We thank A. Artzy-Schinrman, A. Morch and P. Cespedes for comments on the manuscript. We thank L. Campo and the translation histopathology lab for help with multiplex IHC imaging. We thank S. Jones and Oxford Research Biobank for the help with tissue cutting and collection. A national institute for health research (NIHR) academic clinical lectureship supported SS. Oxford human immunology discovery initiative, cancer research UK and LAP (liver and pancreas fund) supported SS. An UCB-Oxford Post-doctoral Fellowship supported EAS. He has received grants from the to fund various elements of this work. Wellcome Trust Principal Research Fellowship 100262Z/12/Z and a grant from KTRR supported M.L.D.

References

1. Kamisawa T, Wood LD, Itoi T, Takaori K. Pancreatic cancer. The Lancet **2016**;388(10039):73-85.
2. Conroy T, Hammel P, Hebbar M, Ben Abdelghani M, Wei AC, Raoul J-L, *et al.* FOLFIRINOX or gemcitabine as adjuvant therapy for pancreatic cancer. New England Journal of Medicine **2018**;379(25):2395-406.
3. De Santiago I, Yau C, Heij L, Middleton MR, Markowetz F, Grabsch HI, *et al.* Immunophenotypes of pancreatic ductal adenocarcinoma: Meta-analysis of transcriptional subtypes. International journal of cancer **2019**.
4. Ino Y, Yamazaki-Itoh R, Shimada K, Iwasaki M, Kosuge T, Kanai Y, *et al.* Immune cell infiltration as an indicator of the immune microenvironment of pancreatic cancer. British journal of cancer **2013**;108(4):914-23.
5. Clark CE, Hingorani SR, Mick R, Combs C, Tuveson DA, Vonderheide RH. Dynamics of the immune reaction to pancreatic cancer from inception to invasion. Cancer research **2007**;67(19):9518-27.
6. Knudsen ES, Vail P, Balaji U, Ngo H, Botros IW, Makarov V, *et al.* Stratification of pancreatic ductal adenocarcinoma: combinatorial genetic, stromal, and immunologic markers. Clinical Cancer Research **2017**;23(15):4429-40.
7. Bayne LJ, Beatty GL, Jhala N, Clark CE, Rhim AD, Stanger BZ, *et al.* Tumor-derived granulocyte-macrophage colony-stimulating factor regulates myeloid inflammation and T cell immunity in pancreatic cancer. Cancer cell **2012**;21(6):822-35.
8. Brahmer J, Reckamp KL, Baas P, Crinò L, Eberhardt WE, Poddubskaya E, *et al.* Nivolumab versus docetaxel in advanced squamous-cell non–small-cell lung cancer. New England Journal of Medicine **2015**;373(2):123-35.
9. Robert C, Schachter J, Long GV, Arance A, Grob JJ, Mortier L, *et al.* Pembrolizumab versus ipilimumab in advanced melanoma. New England Journal of Medicine **2015**;372(26):2521-32.
10. Aglietta M, Barone C, Sawyer M, Moore M, Miller Jr W, Bagalà C, *et al.* A phase I dose escalation trial of tremelimumab (CP-675,206) in combination with gemcitabine in chemotherapy-naive patients with metastatic pancreatic cancer. Annals of oncology **2014**;25(9):1750-5.
11. Beatty GL, Torigian DA, Chiorean EG, Saboury B, Brothers A, Alavi A, *et al.* A phase I study of an agonist CD40 monoclonal antibody (CP-870,893) in combination with gemcitabine in patients with advanced pancreatic ductal adenocarcinoma. Clinical cancer research **2013**;19(22):6286-95.
12. O'Reilly EM, Oh D-Y, Dhani N, Renouf DJ, Lee MA, Sun W, *et al.* Durvalumab with or without tremelimumab for patients with metastatic pancreatic ductal adenocarcinoma: a phase 2 randomized clinical trial. JAMA oncology **2019**;5(10):1431-8.
13. Carstens JL, De Sampaio PC, Yang D, Barua S, Wang H, Rao A, *et al.* Spatial computation of intratumoral T cells correlates with survival of patients with pancreatic cancer. Nature communications **2017**;8(1):1-13.
14. Wartenberg M, Zlobec I, Perren A, Koelzer VH, Gloor B, Lugli A, *et al.* Accumulation of FOXP3+ T-cells in the tumor microenvironment is associated with an epithelial-mesenchymal-transition-type tumor budding

phenotype and is an independent prognostic factor in surgically resected pancreatic ductal adenocarcinoma. Oncotarget **2015**;6(6):4190.
15. Pandol S, Edderkaoui M, Gukovsky I, Lugea A, Gukovskaya A. Desmoplasia of Pancreatic Ductal Adenocarcinoma. Clinical Gastroenterology and Hepatology **2009**;7(11, Supplement):S44-S7 doi https://doi.org/10.1016/j.cgh.2009.07.039.
16. Khaled YS, Ammori BJ, Elkord E. Increased Levels of Granulocytic Myeloid-Derived Suppressor Cells in Peripheral Blood and Tumour Tissue of Pancreatic Cancer Patients. Journal of Immunology Research **2014**;2014:879897 doi 10.1155/2014/879897.
17. Pillay J, Tak T, Kamp VM, Koenderman L. Immune suppression by neutrophils and granulocytic myeloid-derived suppressor cells: similarities and differences. Cell Mol Life Sci **2013**;70(20):3813-27 doi 10.1007/s00018-013-1286-4.
18. Singhal S, Bhojnagarwala Pratik S, O'Brien S, Moon Edmund K, Garfall Alfred L, Rao Abhishek S, *et al.* Origin and Role of a Subset of Tumor-Associated Neutrophils with Antigen-Presenting Cell Features in Early-Stage Human Lung Cancer. Cancer Cell **2016**;30(1):120-35 doi https://doi.org/10.1016/j.ccell.2016.06.001.
19. Panni RZ, Sanford DE, Belt BA, Mitchem JB, Worley LA, Goetz BD, *et al.* Tumor-induced STAT3 activation in monocytic myeloid-derived suppressor cells enhances stemness and mesenchymal properties in human pancreatic cancer. Cancer Immunology, Immunotherapy **2014**;63(5):513-28 doi 10.1007/s00262-014-1527-x.
20. Hsu BE, Tabariès S, Johnson RM, Andrzejewski S, Senecal J, Lehuédé C, *et al.* Immature low-density neutrophils exhibit metabolic flexibility that facilitates breast cancer liver metastasis. Cell reports **2019**;27(13):3902-15. e6.
21. Burel JG, Pomaznoy M, Lindestam Arlehamn CS, Weiskopf D, da Silva Antunes R, Jung Y, *et al.* Circulating T cell-monocyte complexes are markers of immune perturbations. Elife **2019**;8:e46045 doi 10.7554/eLife.46045.
22. Pangrazzi L, Weinberger B. T cells, aging and senescence. Experimental Gerontology **2020**;134:110887 doi https://doi.org/10.1016/j.exger.2020.110887.
23. Pereira BI, De Maeyer RPH, Covre LP, Nehar-Belaid D, Lanna A, Ward S, *et al.* Sestrins induce natural killer function in senescent-like CD8+ T cells. Nature Immunology **2020**;21(6):684-94 doi 10.1038/s41590-020-0643-3.
24. Liu X, Hoft DF, Peng G. Senescent T cells within suppressive tumor microenvironments: emerging target for tumor immunotherapy. The Journal of Clinical Investigation **2020**;130(3):1073-83.
25. Ghorani E, Reading JL, Henry JY, Massy MRd, Rosenthal R, Turati V, *et al.* The T cell differentiation landscape is shaped by tumour mutations in lung cancer. Nature Cancer **2020**;1(5):546-61 doi 10.1038/s43018-020-0066-y.
26. Fourcade J, Sun Z, Chauvin J-M, Ka M, Davar D, Pagliano O, *et al.* CD226 opposes TIGIT to disrupt Tregs in melanoma. JCI Insight **2018**;3(14) doi 10.1172/jci.insight.121157.
27. Fuhrman CA, Yeh W-I, Seay HR, Saikumar Lakshmi P, Chopra G, Zhang L, *et al.* Divergent Phenotypes of Human Regulatory T Cells Expressing the Receptors TIGIT and CD226. The Journal of Immunology **2015** doi 10.4049/jimmunol.1402381.

28. Joller N, Lozano E, Burkett PR, Patel B, Xiao S, Zhu C, *et al.* Treg cells expressing the coinhibitory molecule TIGIT selectively inhibit proinflammatory Th1 and Th17 cell responses. Immunity **2014**;40(4):569-81 doi 10.1016/j.immuni.2014.02.012.
29. Peng J, Sun BF, Chen CY, Zhou JY, Chen YS, Chen H, *et al.* Single-cell RNA-seq highlights intra-tumoral heterogeneity and malignant progression in pancreatic ductal adenocarcinoma. Cell Res **2019**;29(9):725-38 doi 10.1038/s41422-019-0195-y.
30. Khan O, Giles JR, McDonald S, Manne S, Ngiow SF, Patel KP, *et al.* TOX transcriptionally and epigenetically programs CD8+ T cell exhaustion. Nature **2019**;571(7764):211-8 doi 10.1038/s41586-019-1325-x.
31. Zheng C, Zheng L, Yoo J-K, Guo H, Zhang Y, Guo X, *et al.* Landscape of Infiltrating T Cells in Liver Cancer Revealed by Single-Cell Sequencing. Cell **2017**;169(7):1342-56.e16 doi https://doi.org/10.1016/j.cell.2017.05.035.
32. Zhang Y, Lazarus J, Steele NG, Yan W, Lee H-J, Nwosu ZC, *et al.* Regulatory T cell depletion alters the tumor microenvironment and accelerates pancreatic carcinogenesis. Cancer Discovery **2020**:CD-19-0958 doi 10.1158/2159-8290.Cd-19-0958.
33. Kasakovski D, Xu L, Li Y. T cell senescence and CAR-T cell exhaustion in hematological malignancies. J Hematol Oncol **2018**;11(1):91- doi 10.1186/s13045-018-0629-x.
34. Zhao Y, Shao Q, Peng G. Exhaustion and senescence: two crucial dysfunctional states of T cells in the tumor microenvironment. Cellular & Molecular Immunology **2020**;17(1):27-35 doi 10.1038/s41423-019-0344-8.
35. Liu X, Mo W, Ye J, Li L, Zhang Y, Hsueh EC, *et al.* Regulatory T cells trigger effector T cell DNA damage and senescence caused by metabolic competition. Nature Communications **2018**;9(1):249 doi 10.1038/s41467-017-02689-5.
36. Butler A, Hoffman P, Smibert P, Papalexi E, Satija R. Integrating single-cell transcriptomic data across different conditions, technologies, and species. Nature Biotechnology **2018**;36(5):411-20 doi 10.1038/nbt.4096.
37. Korsunsky I, Millard N, Fan J, Slowikowski K, Zhang F, Wei K, *et al.* Fast, sensitive and accurate integration of single-cell data with Harmony. Nature Methods **2019**;16(12):1289-96 doi 10.1038/s41592-019-0619-0.
38. Yang C, Siebert JR, Burns R, Gerbec ZJ, Bonacci B, Rymaszewski A, *et al.* Heterogeneity of human bone marrow and blood natural killer cells defined by single-cell transcriptome. Nature Communications **2019**;10(1):3931 doi 10.1038/s41467-019-11947-7.

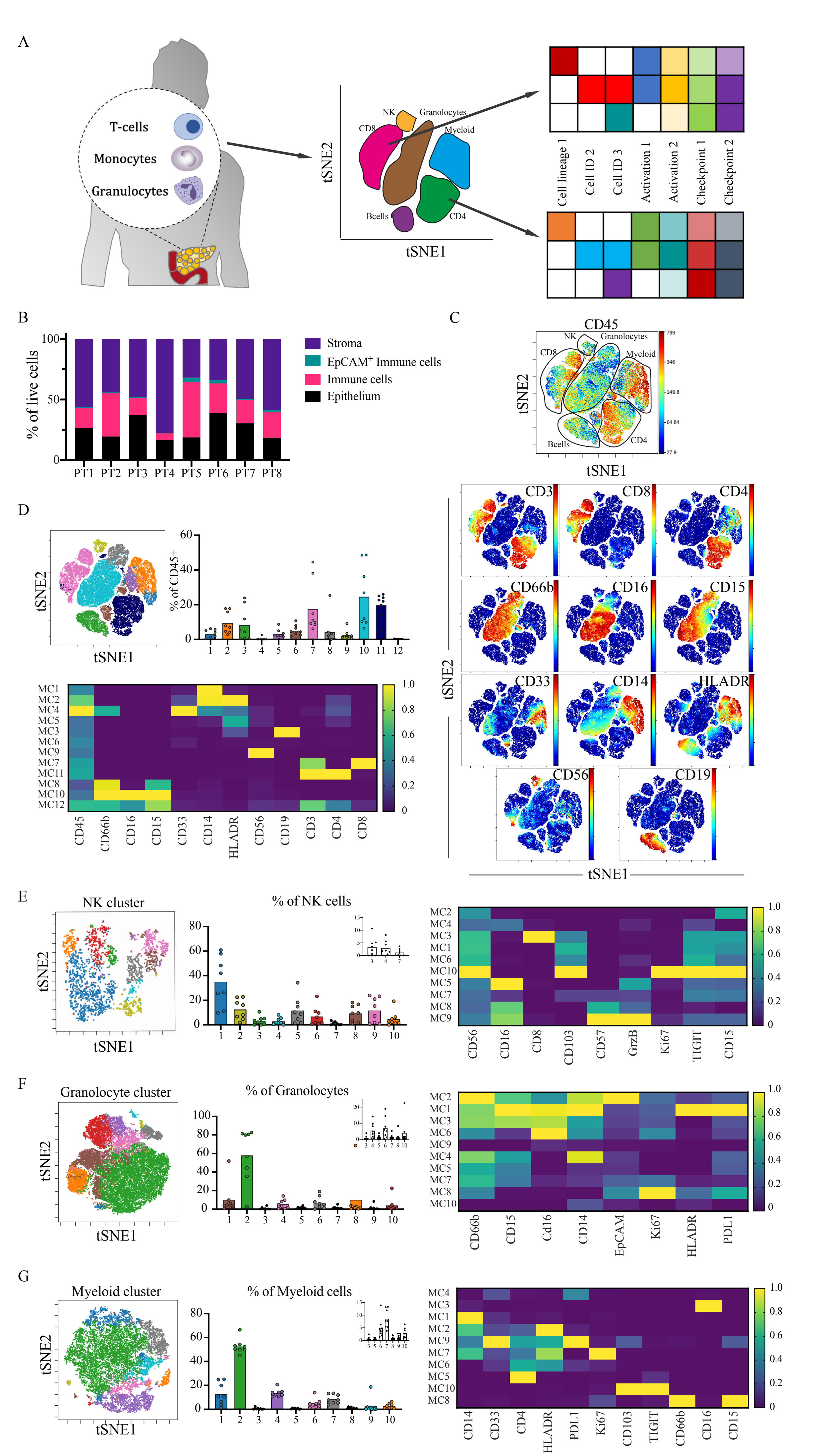

Figure 1, Sivakumar and Abu-Shah et al

Figures

Figure 1: Immune infiltration into PDAC is heterogenous but with a marked T-cell population and suppressive innate cells. (A) Schematics of the experimental procedure; primary resectable pancreatic tumours are made into single-cell suspensions and taken for phenotyping using mass cytometry (CyTOF). CyTOF data was clustered using cytobank Flowsom to identify common populations across patients. Using a set of lineage markers, checkpoints and activation markers cellular states and functionality are defined with a focus on T-cell populations. (B) 200,000 cells pooled from 8 patients were gated in silico and cellular granularity was assessed; Immune cells as (CD45+), EpCAM+ are epithelial cells and double negatives are stroma (including fibroblasts). (C) 100,000 CD45+ cells pooled from 8 patients and viSNE analysis using main cell lineage markers was performed to identify the main immune cell populations. viSNE plot is shown with manual annotation of cell identities (top), expression profile of the CyTOF markers used for clustering is shown (bottom). (D) viSNE plot of the main immune populations coloured and labelled by Flowsom. Bar plots of metacluster frequencies in each patient. Heatmap of Flowsom metaclusters of CD45+ cells; rows represent metaclusters from combined single cells across patients. (E) NK cells were clustered with Flowsom and 10 different metaclusters identified. Metacluster's relative frequency is presented in the bar plot. Inset shows the lower frequency metaclusters . Expression profile for each metacluster is shown in the heatmap (right). The major metacluster being a CD8+ NK population. (F) Granulocyte were clustered with Flowsom and 10 different metaclusters identified. Metacluster's relative frequency is presented in the bar plot. Inset shows the lower frequency metaclusters. Expression profile for each metacluster is shown in the heatmap (right). The major metacluster expressing an intermediate level of CD16 and CD15. Inset shows the lower frequency clusters. (G) Myeloid cells were clustered with Flowsom and 10 different metaclusters identified. Metacluster's relative frequency is presented in the bar plot. Inset shows the lower frequency metaclusters. Expression profile for each metacluster is shown in the heatmap (right). The major metacluster expressing an intermediate level of CD14 and CD33 but high for MHCII (HLA-DR), and another important cluster is the one lacking HLA-DR expression (MSDC). Inset shows the lower frequency metaclusters. All bar plots are median and the individual dots are individual patients. Heatmaps are normalised for each marker.

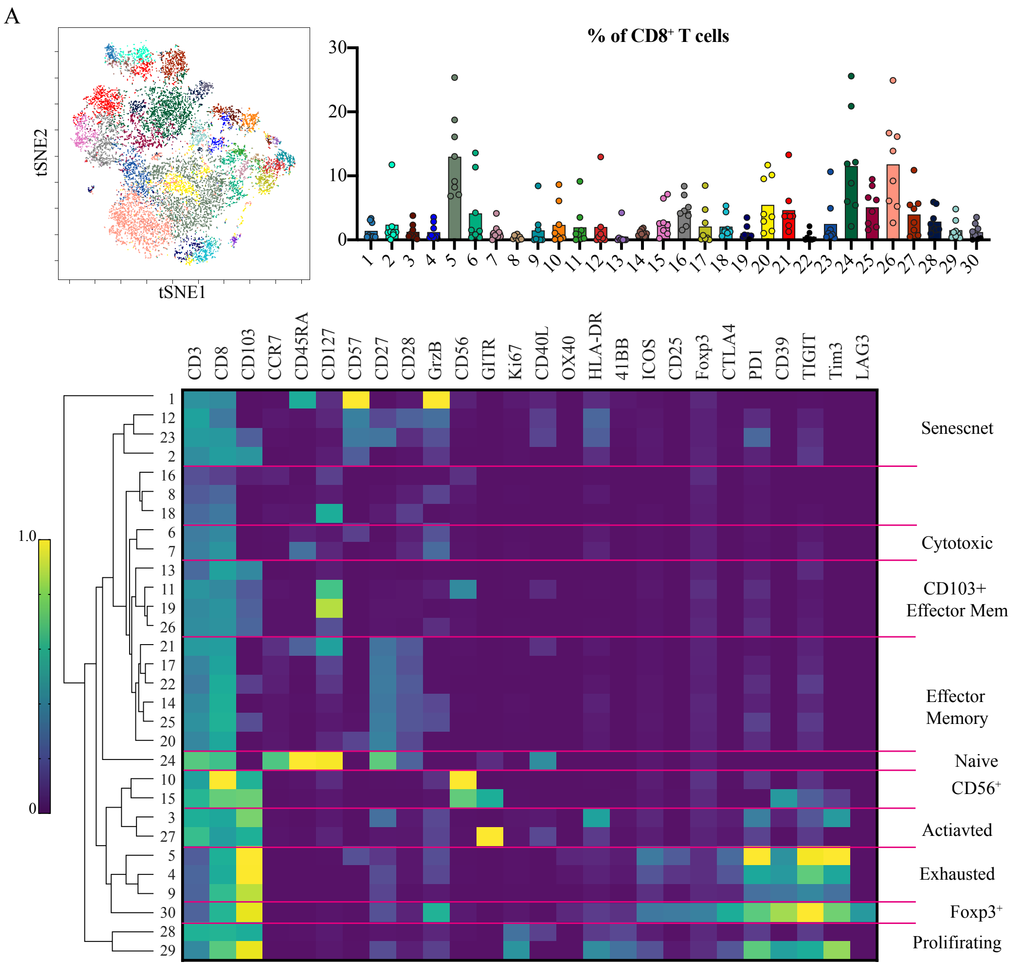

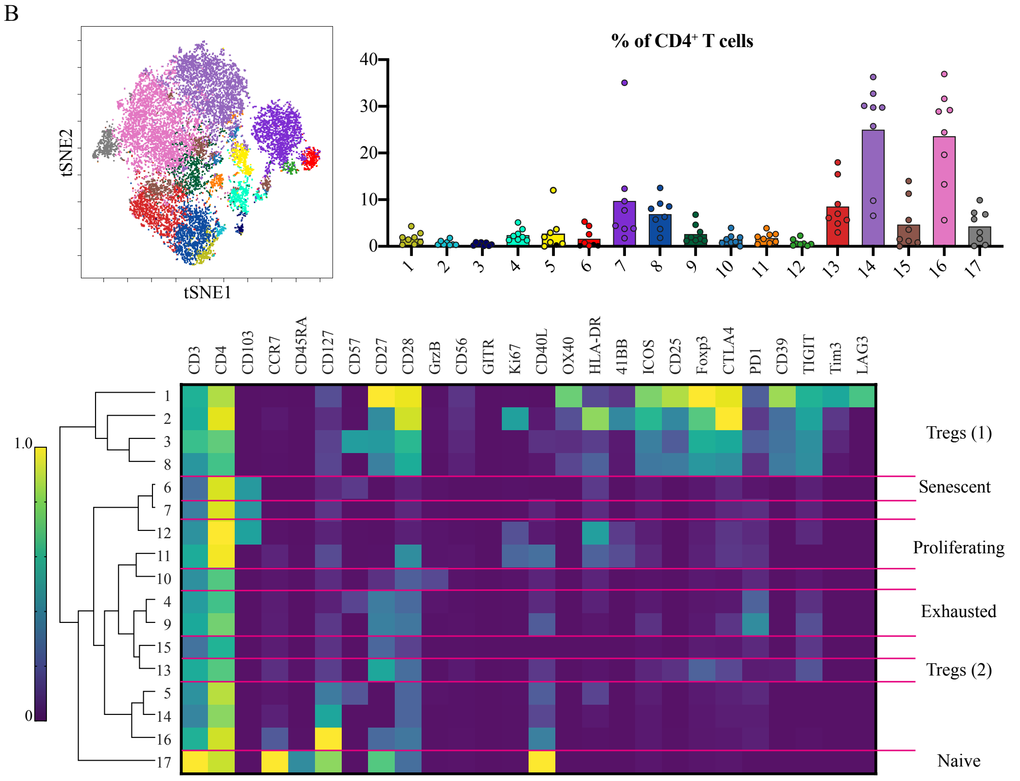

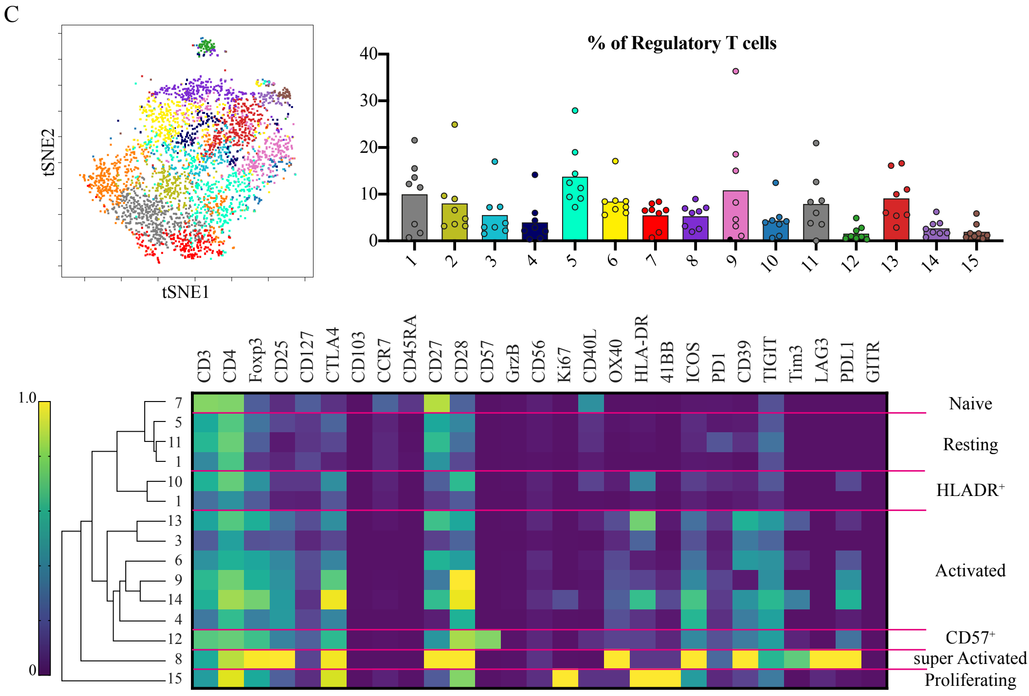

Figure 2, Sivakumar and Abu-Shah et al

Figure 2: CD8 senescence and activate Regulatory T-cells dominate the landscape of the tumour. (A) ~14,750 $CD8_+$ T-cells were pooled and 30 metaclusters identified with Flowsom and visualised on viSNE plot. Metaclusters' relative abundance is shown in the bar plot. The heatmaps show the expression profile of immune checkpoints in the different metaclusters and identified unique populations based on the combinatorial expression. Note that the major $CD8_+$ populations are effector memory cells and the presence of 4 metaclusters corresponding to senescent cells. There is also a proportion of exhausted cells as well as metaclusters of activated cells. (B) ~17,870 $CD4_+$ T-cells were pooled and 17 metaclusters identified with Flowsom and visualised on viSNE plot. Metaclusters' relative abundance is shown in the bar plot. The heatmaps show the expression profile of immune checkpoints in the different metaclusters and identified unique populations based on the combinatorial expression. The major populations are central memory cells, and there were 5 clusters identified as regulatory T-cell (analysed in depth in (C)). (C) ~3,900 $CD4_+$ regulatory T-cells were pooled and 15 metaclusters identified with Flowsom and visualised on viSNE plot. Metaclusters' relative abundance is shown in the bar plot. The heatmaps show the expression profile of immune checkpoints in the different metaclusters and identified unique populations based on the combinatorial expression. More than 50% of the cluster show an activated phenotype albeit at different magnitudes. Bar plots are medians and each dot represents a patient. Heatmaps were normalised across all T-cell populations per marker. Hierarchal clustering of heatmaps was done in Morpheus.

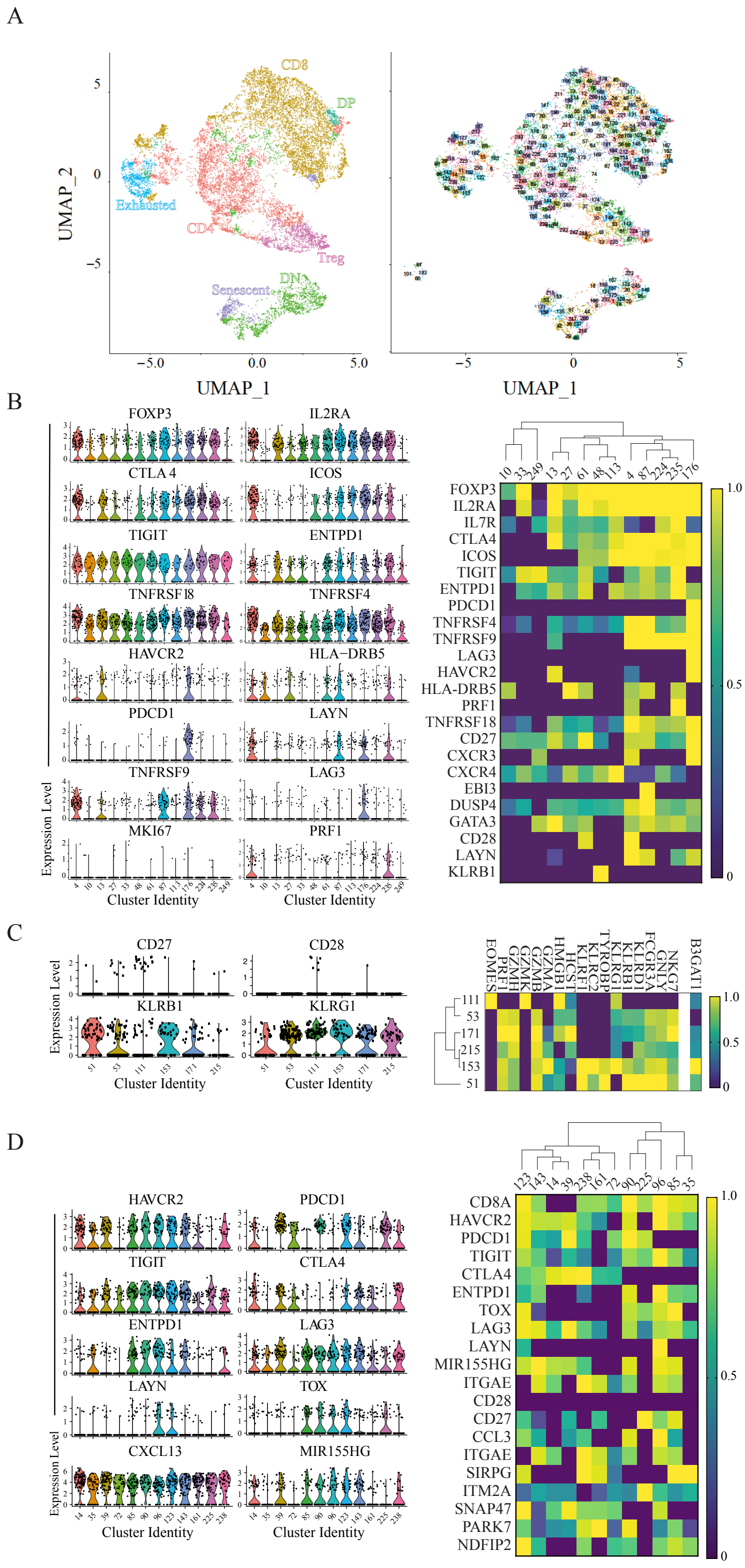

Figure 3, Sivakumar and Abu-Shah et

Figure 3: Single Cell RNA sequencing reveals senescence and regulatory signature of T-cells. (A) (Left) ~13,600 T cells in tumour are projected on UMAP and clusters annotated by the major compartments including regulatory T-cell (pink), senescent T-cells (purple) and exhausted T-cells (cyan). Right, UMAP of the cluster identities in each of the major subsets. (B) (left) Violin plots depicting the 75th percentile scaled expression of the marker genes in the Treg metaclusters and (right) heatmaps showing the top differentially expressed genes in the Treg metaclusters. Expression has been normalised per gene. (C) (left) Violin plots of the 75th percentile expression of the key gene signature for the senescent population. (Right) Heatmaps showing NK and senescence genes uniquely expressed in the senescent population. Heatmap scale for *B3GAT1* is presented as mean values per cluster rather than the 75th percentile due to low capture of this gene. (D) (left) Violin plots of the 75th percentile expression of the key gene signatures for the exhausted T-cell population and (right) the corresponding heatmaps of the key gene signatures. Full expression profiles per cluster is provided in supplementary data file 2.

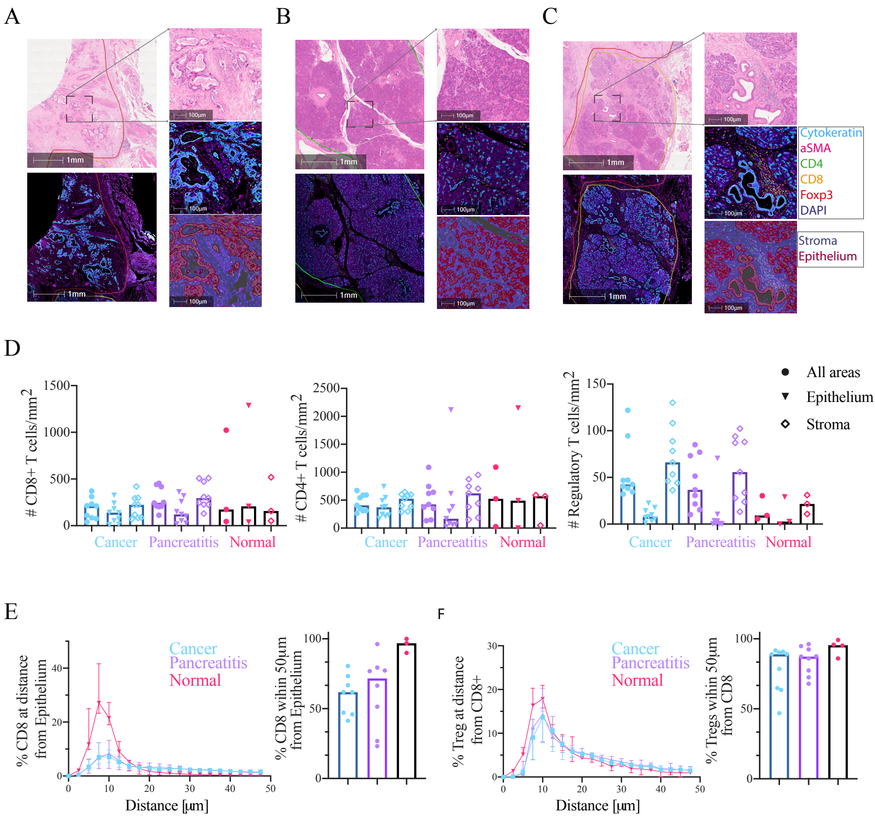

Figure 4, Sivakumar and Abu-Shah et al

Figure 4: Multiplex imaging of T-cell distribution within PDAC tumours identifies a stroma restricted Treg compartment. (A) Cancer region showing (left) H&E (top) at 2x magnification with corresponding immunofluorescence (bottom). (Right) 10x of a region from (left) showing H&E staining (top), the fluorescence signal (middle) and the region classification into epithelium and stroma (bottom). (B) As in (A) for a pancreatitis region. (C) As in (A) for a normal pancreas. (D) Infiltration of $CD8_+$ T-cells (left), $CD4_+$ T-cells (middle) and Tregs (right) into the tissue (Cancer, Pancreatitis and Normal), as well as sub-tissue architectural distribution between the epithelium-rich and stroma-rich areas. (E) Proximity analysis of $CD8_+$ T-cells distance distribution within 50 μm of epithelial cells. (F) Proximity analysis of Treg distance distribution within 50 μm of $CD8_+$ T-cells